A method to model crystalline anisotropy in contact using semi-analytical method

Thibault Beyer, Thibaut Chaise, Julien Leroux, Farshid Sadeghi, Daniel Nelias

A method to model crystalline anisotropy in contact using semi-analytical method

Thibault BEYER[a,b], Thibaut CHAISE[a], Julien LEROUX[b], Farshid SADEGHI[c], Daniel NELIAS[1a]

[a] *Univ Lyon,INSA-Lyon,CNRS UMR5259,LaMCoS,F-69621,France*
[b] *Safran Aircraft Engines, Centre de Villaroche, 77550 Moissy Cramayel, FRANCE*
[c] *School of Mechanical Engineering, Purdue University, West Lafayette, IN 47907, USA*

Abstract

In this paper, the contact problem between a cylinder and a half-space with a crystalline anisotropic behavior is solved. The model is based on semi-analytical methods to solve a three dimensional contact problem. A numerical technique based on a Voronoi tessellation is implemented using the Eshelby's equivalent inclusion method to account for the effect of the material microstructure on the contact pressure distribution and subsurface stresses. Fast Fourier Transforms (3D and 2D) are used to reduce the computation cost of the simulations. An application of this method to compute the scatter in fatigue life of rolling element bearings is also presented. Three different critical stresses are used in the Lundberg-Palmgren equation and results are compared in term of Weibull plot slope.

Keywords: Contact Mechanics, Semi-Analytical Methods (SAM), Voronoi tessellation, Rolling Contact Fatigue (RCF), Eshelby's Equivalent Inclusion Method (EIM), Inhomogeneity, Eigenstrain

1. Introduction

Life of rolling element bearings, used to transmit load between machine components, is mainly limited by a phenomenon called rolling contact fatigue

[1] corresponding author, daniel.nelias@insa-lyon.fr

(RCF) [1]. The main differences between classical fatigue and RCF are the multiaxial state of stress and the moving load during the rolling cycles.

RCF results in two main kind of failure : Surface originated failure called pitting and subsurface originated failure called spalling [2, 3]. Moreover, subsurface cracks have been found to initiate at a depth corresponding to the region of the maximum shear stress reversal [4, 5].

Based on the work of Weibull [6], Lundberg and Palmgren [7] proposed one of the first theories to estimate bearing life. This theory is based on the assumption that the most probable event leading to the bearing failure is subsurface crack initiation mainly due to the presence of a weak point in a volume of material. They hypothesized that the shear stress reversal coming from the contact loading is the main factor of bearing failure. The weak points are assumed to be randomly distributed in the material and the probability of survival of the volume was experimentally found to follow a Weibull distribution [5].

For a bearing under repeated rolling contact loading, the probability of survival S is expressed in the following equation:

$$ln\left(\frac{1}{S}\right) = A\frac{N^e \tau^c V}{z^h} \tag{1}$$

With N the number of repeated loading cycles, τ the maximum value of the shear stress reversal over the stressed volume V and z the corresponding depth. The Weibull slope e, c and h are material dependent parameters and A is an empirical constant.

Modifications of the Lundberg-Palmgren equation have been proposed by several authors in the literature [8–12]. In all these models, the critical stress and its depth are supposed constant to determine the bearing life. But several authors [13, 14] found that, under the same experimental conditions, cracks appear at different depths. The microstructure of steel used in roller bearings, like AISI 52100, is composed of an aggregate of grains (of Ferrite, Austenite, Martensite etc.). The polycrystalline microstructure of 52100 steel can be observed on a fracture surface in Fig. 1. It is important to note that fracture seems

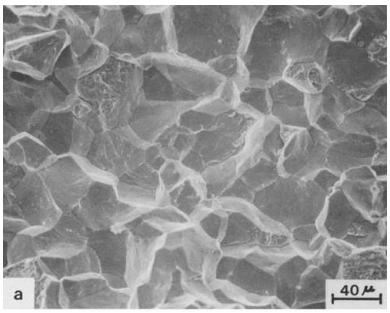

Figure 1: Fracture surface of AISI 52100 steel austenized at 800° [16].

to happen at the grain boundaries [5]. These phenomena can not be taken into account in numerical simulations when considering materials as homogeneous.

Raje et al. [15] proposed an opposite viewpoint by considering that the variation in the critical stress and depth due to the material microstructure are responsible for the dispersion in bearing life. Instead of assuming a Weibull distribution, they simulated randomly generated microstructure topology using a Voronoi tessellation. Moreover, simulating a large number of microstructures allows to reproduce scatter in rolling bearing life. In Raje et al. [15] formulation, the probability of survival and the bearing geometry are considered constant allowing to write a modified bearing life equation:

$$N \propto \frac{z^r}{\tau^q} \tag{2}$$

with $r = 2.33$ and $q = 10.33$ as in Lundberg-Palmgren theory.

The Voronoi tessellation method allows to accurately simulate crystalline material microstructure [17] and has been extensively used to account for microstructure typology randomness in materials for computational homogenization [18, 19]. Raje et al. [20] applied the Voronoi tessellation to rolling contact fatigue life scatter using the finite element method. This model was later extended to 3D simulation [21], crystal elasticity in 2D [22] and in 3D [23]. Moreover, Paulson et al. [24] coupled the FE Voronoi model with an EHL contact resolution. The same method has been applied to fretting contact [25–27] and

coupled with damage model for fretting fatigue [28] and fretting wear [29, 30]. The same approach with multigrid methods based on the work of Brandt [31] and using finite difference technique has been applied for heterogenenous materials by Boffy et al. [32, 33]. Recently, Vijay et al. [34] coupled a cohesive elements Voronoi model with a damage model to compute both the initiation and propagation life of bearings. Ghodrati et al. [35] also presented an approach with cohesive elements and using a crystal plasticity model. Singh et al. [36] applied the same method to determine the effect of surface roughness on tension fatigue. A similar technique have been used to simulate the influence of microstructure and inclusions in gears [37, 38] and in nitrided mechanical parts [39].

Fast and accurate computation of 3D heterogeneous contact problem with a moving load has been allowed through the recent progresses in the development of semi-analytical methods by Nelias and co-workers [40–46] and by the group of Prof. Wang at Northwestern [47, 48]. The Eshelby's formalism has also been implemented to allow the modeling of heterogeneous materials [49–57]. Moreover, the method has been extended to heterogeneous viscoelastic behavior [56, 58] and heterogeneous elastoplastic behavior [59, 60]. Applications to impact [61, 62], repeated rolling [43, 48, 63], and anisotropic homogeneous or layered materials [64–66] have been also proposed.

Recently, development of solutions for thermal inclusion [67] and application to functionally graded thin film [68] and imperfect interface conditions [69] have been presented. A method to take into account damage occurring during fretting and butterfly wings formation around inclusion can be found in [70, 71]. Some application to lubricated contact for rough contact have been proposed in [72] and a coupled heterogeneous EHL solver in [73–75].

The purpose of the present work is to use a voxel technique to model the microstructure of steels generated by a Voronoi tessellation with the semi-analytical method. Grains are discretized in multiple cuboidal inclusions with cubic elastic properties. Eigenstrains of those multiple cuboidal inclusions are generating a disturbance stress field called eigenstress. Effect of eingenstresses

close to the top surface on the pressure distribution has been highlighted in [54]. A similar enrichment technique has been proposed and validated in [56, 57, 70, 71]. Rolling contact simulations have been performed and scatter in fatigue life is estimated. The emphasis is put on the effect of local stress gradient appearing at grain boundaries on the scatter of the maximum critical stress depth. The main difference with the models in the literature [15, 21, 23] is the coupling between the contact problem and the heterogeneous material model.

2. Theoretical Background and model description

2.1. Contribution of subsurface problem in the contact resolution

The three-dimensional contact solution depends on the contact load, the contacting bodies geometry and on the contacting bodies subsurface behavior. Thus, the presence of heterogeneous inclusions inside the material is modifying the contact solution and can be taken into account by using the Eshelby's equivalent inclusion formalism as presented in [40, 54, 55, 57, 59, 70]. The disturbed stress field due to the presence of inclusions inside the material can be converted into eigen-displacements u_z^* induced by these inhomogeneities in the surface separation equation (Eq. (3)) :

$$h(x,y) = h_i(x,y) + \delta + u_z(x,y) + u_z^*(x,y) \tag{3}$$

The following section presents the Eshelby's equivalent inclusion framework and its application to the calculation of Eshelby's eigenstrain ε^* and the corresponding eigendisplacements u_z^* in the case of an elastic half-space containing elastic inhomogeneities. The different steps leading to the computation of the effect of the presence of multiple inclusions inside one of the contacting body have already been presented in [70, 71] and are briefly recalled in Section 2.2.

2.2. Eshelby's equivalent inclusion method in Contact Mechanics

According to Eshelby's framework, an infinite body having an heterogeneity called Ω with elastic properties C_{ijkl}^I is equivalent to an homogeneous body

with an homogeneous inclusion having the elastic properties of the matrix C^M_{ijkl} but subjected to some misfit strains called eigenstrains (ε^*). Those eigenstrains come from the incompatibility of strains between the two different bodies when an external load is applied. Applying the Eshelby's equivalent inclusion method to an elastic isotropic material is giving the consistency equation:

$$C^I_{ijkl}(\varepsilon^0_{kl} + \varepsilon_{kl}) = C^M_{ijkl}(\varepsilon^0_{kl} + \varepsilon_{kl} - \varepsilon^*_{kl}) \quad \text{in } \Omega \tag{4}$$

Eshelby's solution has been extended to multiple interacting inclusions by Moschovidis and Mura [76] and have already been solved by several authors [51, 52, 54, 70, 71] using a conjugate gradient algorithm (CGM) to take into account for the mutual influence between close inclusions.

Eshelby's inclusion method (EIM) has been developped under the assumption of an infinite space. But EIM can be also be applied to an half-space problem by using Chiu's decomposition as proposed by Jacq et al. [40] and later Zhou et al. [49].

In order to determine the stress fields caused by the presence of inhomogeneities, the computational domain is meshed into $n_x \times n_y \times n_z$ cuboids. The stress field is related to the eigenstrains through the equation 5 using the influence coefficients B_{ijkl} and M_{ij} that can be found in Appendix B.

$$\begin{aligned}\sigma_{ij}(x,y,z) = &\sum_{x^I=0}^{n_x-1}\sum_{y^I=0}^{n_y-1}\sum_{z^I=0}^{n_z-1} B_{ijkl}(x-x^I, y-y^I, z-z^I)\varepsilon^*_{kl}(x^I,y^I,z^I) \\ &+ \sum_{z^I=0}^{n_z-1}\sum_{y^I=0}^{n_y-1}\sum_{x^I=0}^{n_x-1} B_{ijkl}(x-x^I, y-y^I, z+z^I)\varepsilon^*_{skl}(x^I,y^I,-z^I) \\ &- \sum_{y^I=0}^{n_y-1}\sum_{x^I=0}^{n_x-1} M_{ij}(x-x^I, y-y^I, z)\sigma^n(x^I,y^I,0)\end{aligned} \tag{5}$$

The computation of the stress field can be accelerated using numerical technique (3D-FFT and 2D-FFT) as proposed by [77, 78].

The stress field σ^n generated at the free surface by the presence of het-

erogeneities is modifying the normal displacement at the free surface of the half-space. Using K^n, the influence coefficients relating the normal pressure to the normal displacement of a rectangular area (see Appendix C), one can find the normal eigen-displacement of the half-space free surface:

$$u_z^*(x,y) = \sum_{y'=0}^{n_y-1} \sum_{x'=0}^{n_x-1} K^n(x-x', y-y')\sigma^n(x',y') \tag{6}$$

Chiu [79] extended Eshelby's work for ellipsoidal geometry to cuboidal inclusions. The present work is using multiple cuboidal inclusions in the half-space as an enrichment technique as already used by the authors in [70, 71].

The proposed heterogeneous semi-analytical contact solver is presented in Fig. 2. The initial conditions are defined by the two contacting bodies geometry and material properties. The loading conditions are imposed through a defined load or displacement. The contact pressure and stress field is found using a conjugate gradient algorithm. The elastic stress field is used as an input to solve Eshelby's equivalent inclusion method and find the eingenstrains. The corresponding eigen-displacements are modifying the contact geometry and the elastic contact solution needs to be updated. This loop is repeated until convergence is obtained on the eigen-displacements.

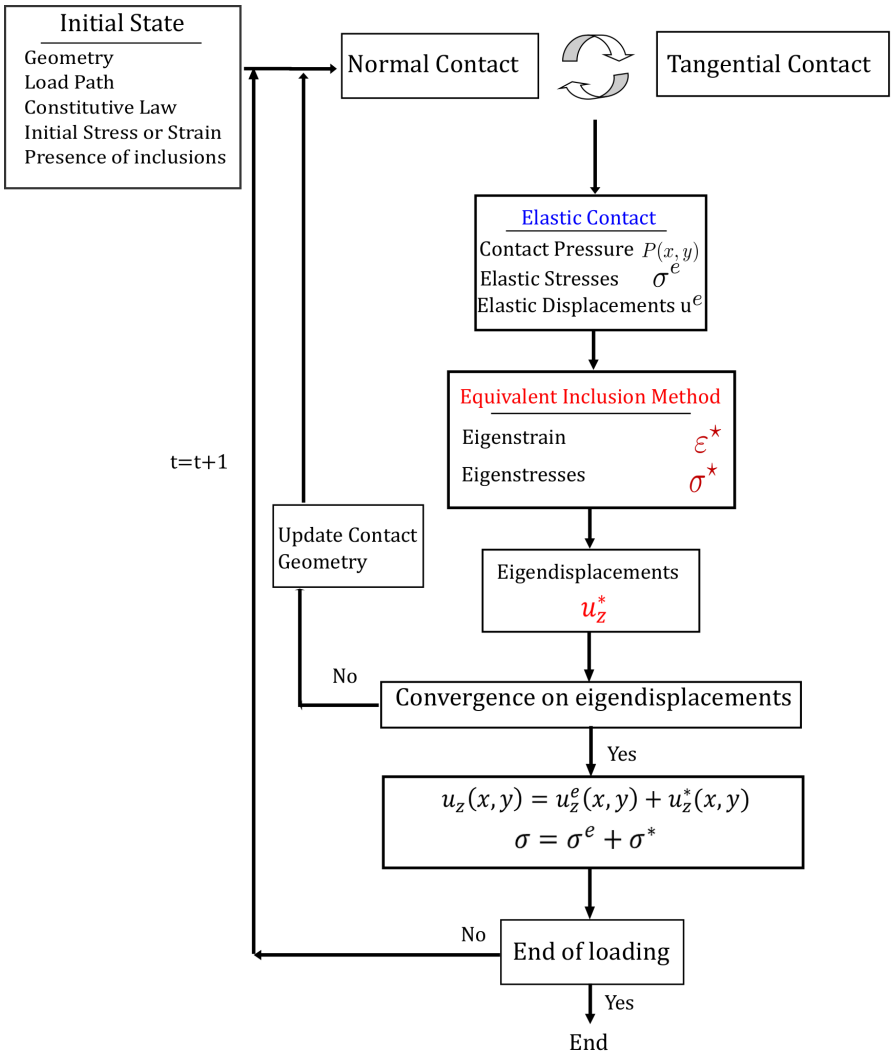

Figure 2: Flow chart for processing the semi-analytical model for elastic contact in presence of inclusions.

3. Modeling polycrystalline anisotropy with SAM

3.1. Voronoi tessellation

The Voronoi tessellation is a numerical technique to divide a continuous space into regions following some principles detailed in Okabe and Boots [80] and recalled here:

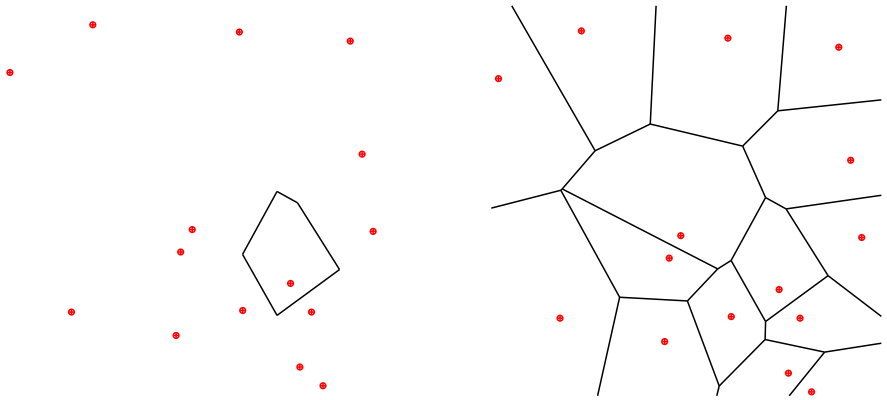

Figure 3: The Voronoi tessellation process: space partition from a 2D seed distribution.

- a set of not coinciding seed points $\gamma = \{p_1, p_2, ..., p_n\}$ are randomly placed in a three dimensional volume $V \in \mathbb{R}^3$.

- The volume V is divided into regions $V_{\{p_i\}}$, volume of influence associated with a seed point p_i. Each region is composed of every point closer (using euclidian distance) to the seed point p_i than to any other seed points of γ. This condition can be expressed for each point $x \in V$:

$$V_{\{p_i\}} = \{d(p_i, x) \leq d(p_j, x), j \in [1, n], \forall x \in V\} \tag{7}$$

- Grain boundaries are the planes formed by the points equidistant from two seed points. Therefore Voronoi cells are convex close polyhedra covering the entire volume V and forming the Voronoi diagram.

The distribution of seed points in the volume allows to capture the randomness in the microstructure topology. Moreover, the density of seed points and their distribution is controlling the average grain size and shapes. A Poisson process is often used to place the seed points because of its ability to accurately reproduce polycrystalline microstructures [21].

The representation of microstructure is limited to the volume where the gradient of stresses from the contact is significant regarding the characteristic length

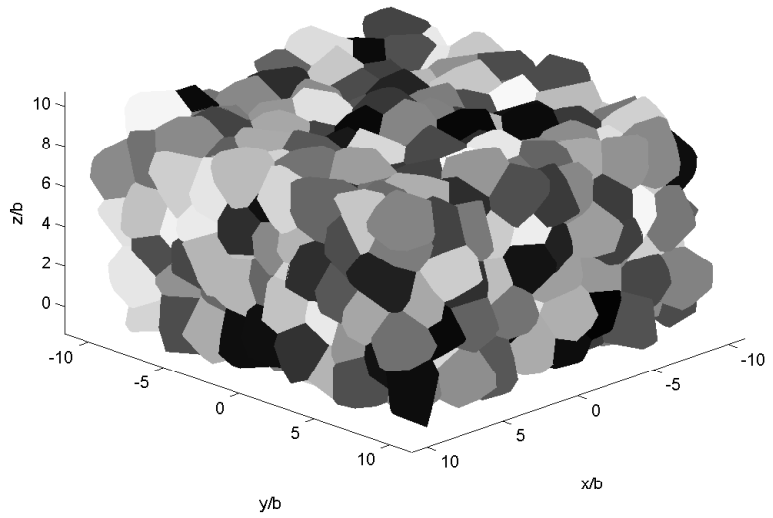

Figure 4: Example of a 3D Voronoi tessellation

of the microstructure. The grain diameter is an input of the algorithm to place the seed points of the Voronoi diagram and using the MATLAB's Voronoi algorithm based on the software QHULL [81]. All the Voronoi diagrams presented in this paper have been generated using a MATLAB's algorithm developed at the METL laboratory of Purdue University.

3.2. Mesh building

In finite element approach, the mesh of the Voronoi diagram is often unstructured and divides Voronoi cells into tetrahedral elements to obtain a fine discretization of the grain boundaries [23]. Another technique consists in using a structured mesh with cubic elements (also called voxel) [26, 27]. Due to the

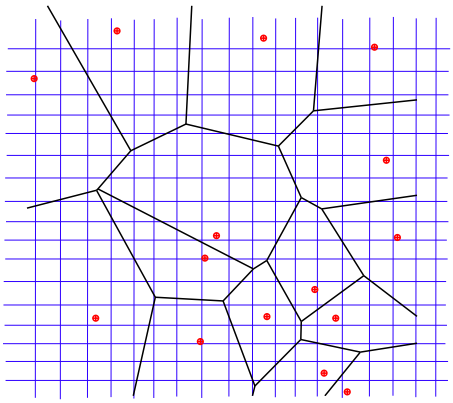

Figure 5: Voxelization of the Voronoi tessellation

discretization used in the semi-analytical solver, this kind of method is chosen here.

The discretization grid of the semi analytical solver is superimposed on the Voronoi diagram (see Fig. 5). Each grid point is then labelled with the Voronoi cell it belongs to. The labelization process is done from the calculation of the minimum distance between the point of the grid and one of the seed points. This process is creating a cubic volume with smooth surfaces at the edges and with each grid point assigned to only one Voronoi cell.

3.3. Polycrystalline anisotropy

Most of the microstructure models in the literature are simulating isotropic materials but on the microstructural scale, steel is made of randomly oriented anisotropic crystal grains. If the loading conditions allow to consider the macroscale response of the material, then the local anisotropy of the grains is resulting in an isotropic global material behavior and stiffness. But considering the high stress gradient in contact loading, the grain orientation needs to be taken into account. A cubic anisotropy model is adopted here to simulate the crystalline elasticity of the material as in Vijay et al. [23]. A single crystal structure is assumed here for sake of simplicity and each grain has the same elastic stiffness constants as recalled in Eq. (8). Each grain has the same stiffness in its local

coordinate system but the macroscopic response of the material is evaluated in the global cartesian reference frame. It is then necessary to rotate the local grain stiffness matrix C_{local} into the reference frame $C_{reference}$ following Eq. (9). Thus, the stiffness of each grain produces different values in the reference frame.

$$\begin{pmatrix} \sigma_{11} \\ \sigma_{22} \\ \sigma_{33} \\ \sigma_{23} \\ \sigma_{31} \\ \sigma_{12} \end{pmatrix} = \begin{pmatrix} C_{11} & C_{12} & C_{12} & 0 & 0 & 0 \\ C_{12} & C_{11} & C_{12} & 0 & 0 & 0 \\ C_{12} & C_{12} & C_{11} & 0 & 0 & 0 \\ 0 & 0 & 0 & C_{44} & 0 & 0 \\ 0 & 0 & 0 & 0 & C_{44} & 0 \\ 0 & 0 & 0 & 0 & 0 & C_{44} \end{pmatrix} \begin{pmatrix} \varepsilon_{11} \\ \varepsilon_{22} \\ \varepsilon_{33} \\ 2\varepsilon_{23} \\ 2\varepsilon_{31} \\ 2\varepsilon_{12} \end{pmatrix} \tag{8}$$

$$C_{reference} = R_{Z''} R_{X'} R_Z C_{local} R_Z^T R_{X'}^T R_{Z''}^T \tag{9}$$

In the simulation, random Euler angles are assigned to each cell of the Voronoi diagram. The regular grid is superimposed on the Voronoi diagram and each point of the discretization grid is assigned to a Voronoi cell (see section 3.2). Therefore each grain is discretized in small cuboid. One should note that multiple cuboids are representing a grain (see Fig. 5). Each grain is filled with small cuboidal inclusions having the same size than the discretization size. All the inclusions inside one single grain have the same cubic elastic properties but rotated accordingly with the assigned angles of the grain. Thus all the inclusions belonging to a specific grain have the same rotation angles. A flow chart summing up the creation of the polycrystalline domain is presented in Fig. 6.

Vitos et al. [82] determined cubic material constant for stainless steel from quantum mechanical calculations and his results are used in the simulations (see Table 1).

A measure of anisotropy is defined through the parameter A [22] and is

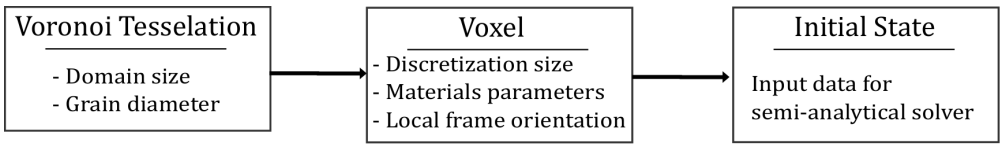

Figure 6: Flow chart for creating a Voronoi tessellation in the semi-analytical model.

Table 1: Cubic elasticity constants for steel [82]

Elastic Constants	**(GPa)**
C11	204.6
C12	137.7
C44	126.2

calculated to be 3.78 here:

$$A = \frac{2C_{44}}{C_{11} - C_{12}} \tag{10}$$

In Fig. 7, the Voronoi diagram is voxelized and random Euler angles are assigned to each grain. It should be noted that this method is also able to simulate textured alloys by giving a principal orientation for every grain of the material.

3.4. Contact stress field in polycrystalline materials

3.4.1. Description of the parameters of the simulation

In this section the rolling contact between a rigid cylinder of radius $R = 2.78$ mm and an heterogeneous half-space is considered. The applied normal load is $W = 25.5$ N and is moving from $X = -b$ to $X = +b$ in 21 increments of distance $\delta X = 0.1b$. With a Young's modulus $E_0 = 200$ GPa and a Poisson ratio $\nu_0 = 0.3$, the contact half width b is equal to 0.05 mm in the X-direction

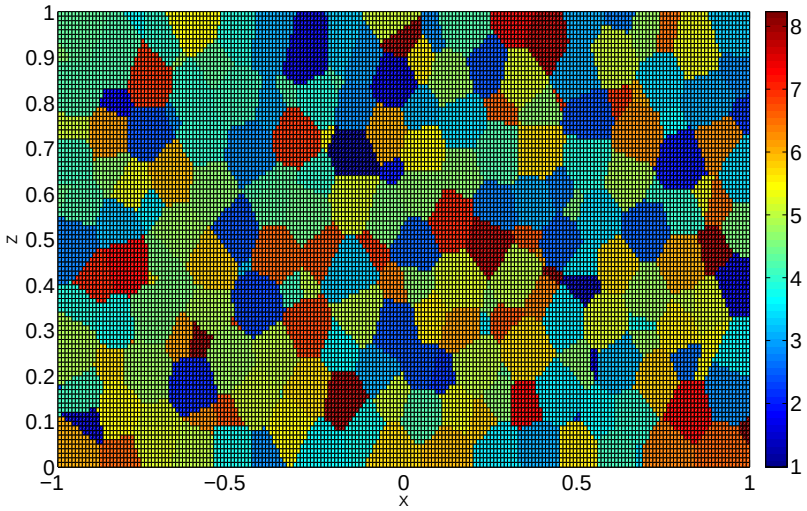

Figure 7: Voxelization of the domain accordingly to the Voronoi tessellation. Amplitudes correspond to the sum of the Euler angles.

and the maximum pressure P_0 is equal to 2 GPa. In this part, the effect of friction was neglected.

One should note that the problem solved here is 3D. The cylinder length in the Y-direction is chosen to be larger than $3b$ and the computation volume is restricted to a size of $2b$ in this direction in order to avoid any side effect from the cylinder geometry.

In order to represent the crystalline microstructure of the material, a Voronoi tesselation is realized following the steps described in Fig. 6. The average grain size in the Voronoi tessellation is around 10 μm [83]. The half-space is then filled with cubic elastic inclusions having the same size as the discretization size (Fig. 8). The microstructure volume is created with smooth free surfaces and no roughness is defined at the interface between the two contacting bodies.

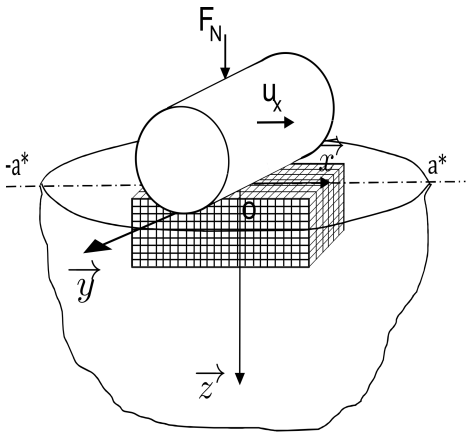

Figure 8: 3D view of a cylinder rolling on a elastic half-space with multiple cuboidal inclusions superposition.

Note that the computation being elastic and without friction, only the randomly oriented microstructure has an influence on the results. The microstructure is made of around 600 000 inclusions. The half-space is discretized in $225 \times 115 \times 59$ computation points such that the space between each points is $2\Delta x = 2\Delta y = 2\Delta z = 0.04b$. The proposed method allows to compute a rolling cycle in around 10 hours with 8 processors at 2.40 GHz and 8 GB RAM. The loading and material parameters used in this section are consistent with the ones from Vijay et al. [23]. The elastic constants of the inclusions are chosen to represent the same steel.

3.4.2. Stress field and contact pressure in the anisotropic domain

The stress field under the contact is strongly affected by the mismatch in the orientation of the cubic structure. The microstructure affects the depth and the amplitude of the maximum stress in the material during a loading cycle. The von Mises stress in the plane $y = 0$ is plotted in Fig. 9b and shows the stress rising effect of inclusion mismatch. The von Mises stress in the anisotropic and in the isotropic domain is plotted along the depth ($z > 0$) in ($x = 0; y = 0$). The von Mises stress amplitude in the anisotropic domain is locally higher than the one in the isotropic domain. The effect of the microstructure can also be observed

on the contact pressure in Fig. 10. The presence of local eigenstresses below the surface is modifiying the surface separation equation (Eq. 3) as explained in section 2.2. Theses changes in the surface geometry result in modifications of the contact pressure distribution. One may note that the maximum pressure is lower in the anisotropic domain than in the isotropic domain and the area of contact is larger in order to conserve the load equilibrium. This may come from the material orientation of the inclusions at the contact surface. The main difference with the work of Vijay et al. [23] is the coupling between the contact solution and the heterogeneous material solver. Vijay et al. [23] used an unstructured meshing of the 3D Voronoi cells and a four point Gauss quadrature scheme. Their Voronoi diagramm is 4b long in every direction and the model was solved using the commercial sofware Abaqus. In Vijay et al. [23], the contact pressure is imposed and assumed Hertzian. In the present results, and with the same imposed normal load, the contact pressure is influenced by the microstructure resulting in a larger contact area and a lower maximum pressure. This larger distribution of pressure on the surface is responsible for a slightly lower stress distribution in the subsurface (see Fig. 9) than what can be observed in Vijay et al. [23]. Finally, the results in Fig. 9 show that the maximum von Mises stress in the anisotropic domain is resulting from the mismatch between the orientation of two grains but is not strongly affecting the contact pressure if it is localized far enough from the top surface.

3.5. Application to fatigue life of rolling bearings

Fatigue is a process of damage accumulation manifesting through decreasing material properties in the solid. It can be decomposed in three steps: initiation of cracks, propagation of the cracks and final rupture of the material. Each step is acting at different speeds depending on the material. The present work is focusing on the initiation of cracks because it is particularly affected by the random distribution of material properties and defects inside the material microstructure [84]. The difference in elastic properties between the crystal acts

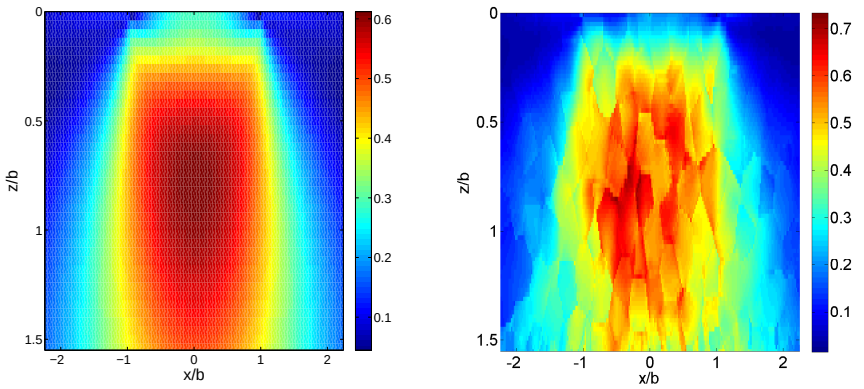

(a) (b)

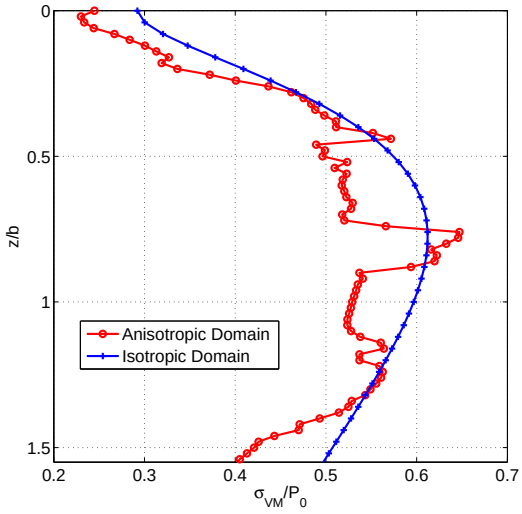

(c)

Figure 9: Dimensionless von Mises stress in the plane $y = 0$ (a) in an isotropic domain (b) in an anisotropic polycrystalline domain. (c) von Mises stress along z direction in the anisotropic domain and in the isotropic domain.

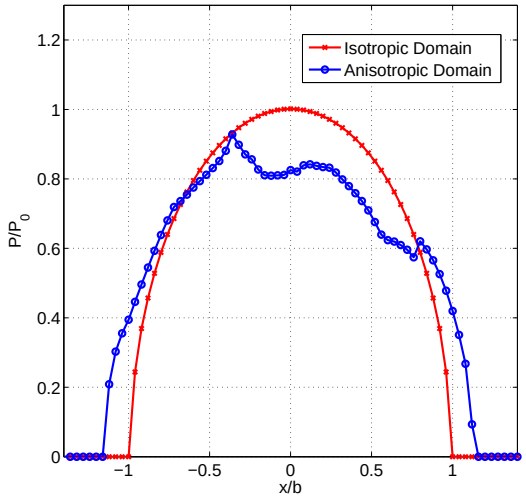

Figure 10: Contact pressure between the rigid cylinder and the isotropic domain and with the anisotropic domain.

as a stress riser in solid and in particular at the grain boundaries [85]. The previous microstructure model is used to predict the location of crack initiation in the material and its fatigue life under contact loading.

3.5.1. Life scatter in rolling element bearings due to microstructure

The critical stress and the corresponding depth are the variable parameters from Eq. 2 that need to be determined in order to calculate the bearing life. Several microstructure simulations are giving life predictions and allow to determine the Weibull slope parameter e. The same approach has already been used with 2D [22, 86] and 3D [23, 87] finite element models. The same method has also been applied to the study of plasticity in rolling contact [88, 89], fretting [29] and formation of butterfly wings [90].

3.5.2. Critical stress computation

As in Vijay et al. [23], numerical simulations have been performed on 30 crystalline domains in order to guarantee a good accuracy in the Weibull distribution [91]. The Voronoi tessellation is the same in every domain and only the

orientation angles of each crystal are changing. Effect of material orientation on the RCF life scatter is analyzed with three different critical stresses: maximum shear stress reversal, maximum Tresca stress and maximum von Mises stress. Amplitude and depth of the maximum critical stress in every domain are compared with the results obtained with an isotropic domain. Results for the maximum shear stress reversal are presented in Fig. 11, for the maximum Tresca stress in Fig. 12 and for the maximum von Mises stress in Fig. 13. For every simulation, the maximum critical stress amplitude found is higher in the anisotropic domain than in the isotropic domain while the corresponding depth is varying around the reference homogeneous isotropic domain value. The mean amplitude of the shear stress reversal is found to be $0.658P_0$ and their depth locations are found to vary between $0.36b$ and $0.68b$. The mean amplitude of the maximum Tresca stress is evaluated at $0.475P_0$ and their depth locations are found to vary between $0.52b$ and $1.04b$. Finally, the mean amplitude of the maximum von Mises stress is found to be $0.849P_0$ and their depth locations are found to vary between $0.56b$ and $1.04b$. For all three critical stresses, results presented here are showing a scatter in the localization of the critical stress between the different anisotropic domains.

3.5.3. Fatigue criterion

According to Raje et al. [15] hypothesis, it is the variation in magnitude and depth of the critical stress that is responsible for the scatter in bearing life. The scatter in the results obtained with 30 different material microstructures is used to create a Weibull plot of the probability of failure. One should note that no Weibull distribution of the fatigue lives is explicitly assumed here. 2 and 3 parameters Weibull plots are realized with the three different critical stresses and are presented in Figs. 14, 15 and 16. The corresponding Weibull slopes and scale parameters can be found in Table 2. The slope of the Weibull plot is giving information about the scatter of the estimated fatigue life (the lower the Weibull slope, the higher is the scatter in the fatigue life) while the scale parameter is giving information about the distribution of the probability

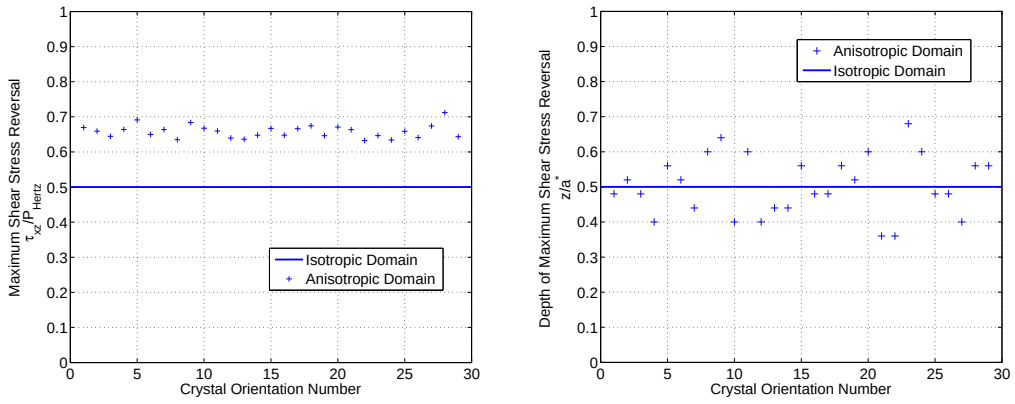

(a) (b)

Figure 11: (a) Variation of magnitude in the maximum shear stress reversal (b) Variation of the corresponding depth in the 30 anisotropic domains.

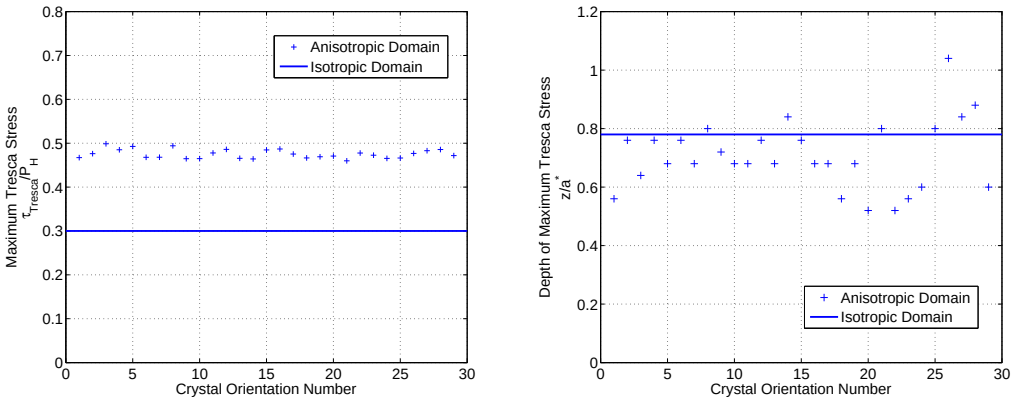

(a) (b)

Figure 12: (a) Variation of magnitude in the maximum Tresca stress (b) Variation of the corresponding depth in the 30 anisotropic domains.

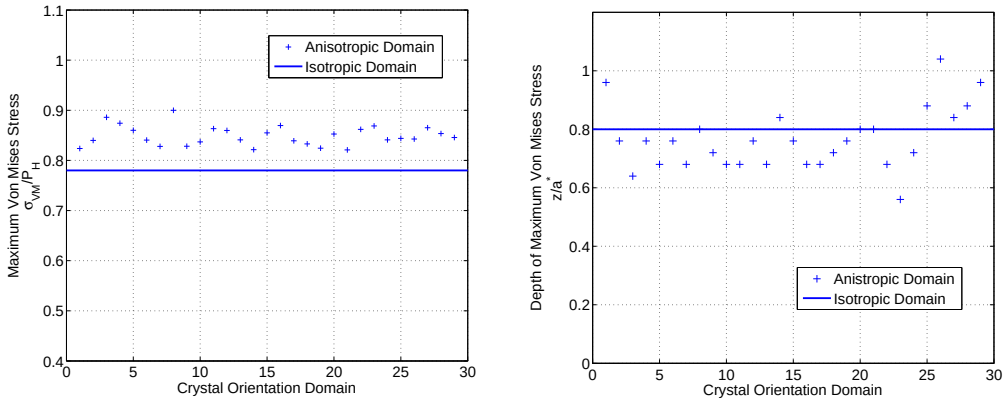

(a) (b)

Figure 13: (a) Variation of magnitude in the maximum von Mises stress (b) Variation of the corresponding depth in the 30 anisotropic domains.

density over time, representing the characteristic life. One can observe that the maximum shear stress is showing the higher slope resulting in a lower scatter than the two other critical stresses. The scale paramater associated with the maximum shear stress is also the lower. The slope of the different Weibull parameters are in the same range. The scale parameter of the maximum Tresca stress is much larger than the scale associated with the two other critical stresses meaning that the estimated life is higher. It is in good agreement with the fact that the mean maximum Tresca stress was found lower than the two other mean critical stresses (see section 3.5.2). Also a vertical distribution of points at the beginning of the Weibull plot as shown in Fig. 15 is giving an indication about a possible minimum fatigue life. Therefore, the numerical data seems to better fit with the 3-Parameters Weibull plot. One should recall that no Weibull distribution was assumed here. The results of the simulations are plotted and fitted with a Weibull plot. These results are confirming the influence of the material microstructure in the life scatter of parts under RCF loading.

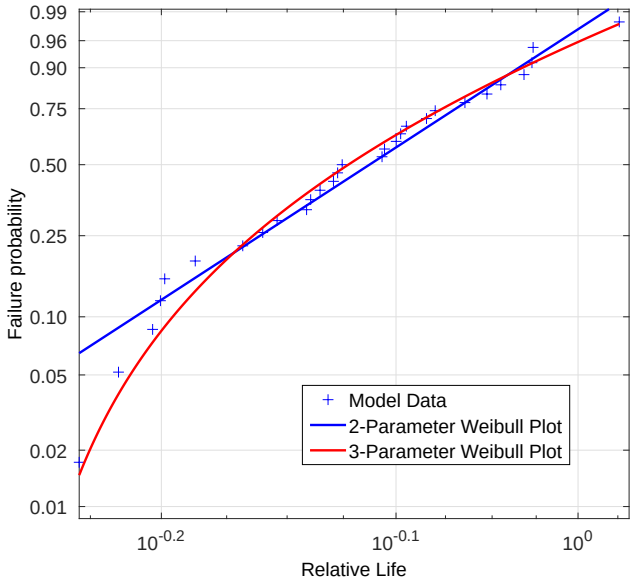

Figure 14: 2 and 3 parameters Weibull plots superimposed on the data from the model for the maximum shear stress reversal criterion.

Table 2: Weibull slopes and scales for different stress criteria.

Stress Criterion	**Parameter**	**2-Param. Weibull plot**	**3-Param. Weibull plot**
$\Delta\tau_{xz}$	Slope	6.5587	2.2899
	Scale	0.8188	1.6255
τ_{Tresca}	Slope	2.4998	1.3268
	Scale	1.15×10^3	3.0×10^3
τ_{VM}	Slope	2.4039	1.5534
	Scale	3.5349	6.6421

3.5.4. Comparison with Weibull slope parameters from finite element simulations

The Weibull slopes obtained with our results are compared with the Weibull slopes found in the literature in Table 3. The presented results are in the same

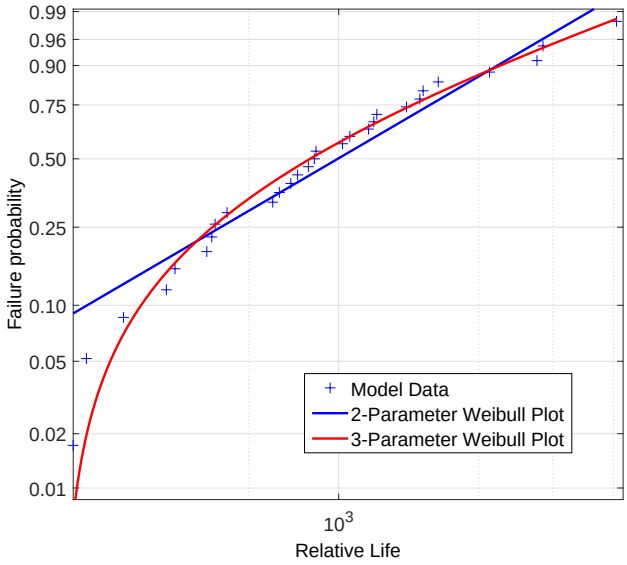

Figure 15: 2 and 3 parameters Weibull plots superimposed on the data from the model for the maximum Tresca stress criterion.

range than the results obtained with finite element models for isotropic and anisotropic materials. The slopes presented here are lower than the ones found by Raje et al. [15] and Weinzapfel et al. [87] who only studied the effect of the microstructure topology without taking into account the effect of material orientation in the grains. The scatter due to the variation in both the topology and the grain orientations have been modeled in 2D by Paulson et al. [22] and in 3D by Vijay et al. [23]. Their results are logically showing an higher scatter. The results presented in Table 2 are in good agreement with the slopes found experimentally by Lundberg and Palmgren [7] and with a finite element approach by Vijay et al.[23]. Using the maximum shear stress reversal, Weibull slopes obtained with the semi-analytical solver exhibit a higher slope than the one found with finite element by Vijay et al. [23]. One reason is that the voxelization of the microstructure doesn't allow to accurately reproduce the smooth grain boundaries [92]. Moreover, the computational discretization of the semi-analytical solver is only able to compute the stress field on a regular

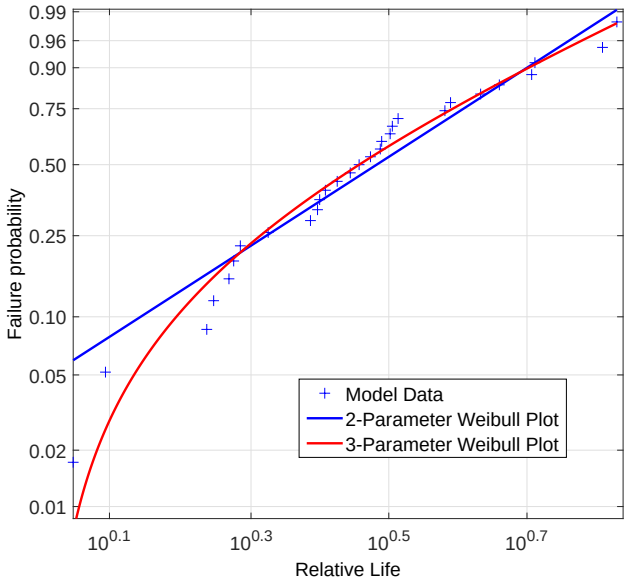

Figure 16: 2 and 3 parameters Weibull plots superimposed on the data from the model for the maximum von Mises stress criterion.

grid of Gaussian points while the finite element model allow to mesh the grains to compute the shear stress reversal on the geometric grain boundary. This difference can be observed in the lower amplitude of the shear stress reversal in Fig. 11a than in Vijay et al. [23].

Furthermore, the coupling between the contact problem and the subsurface problem is also affecting the results in the present work. Finally, the methodology presented here is showing the ability of the semi-analytical solver to capture the life scatter in rolling contact fatigue.

4. Conclusion

A numerical method has been proposed to model the effect of crystalline anisotropy in the rolling contact problem between a rigid cylinder and an heterogeneous half-space. A three dimensional heterogeneous elastic contact solver is used based on the Eshelby's equivalent inclusion method. A method of space

Table 3: Weibull slopes from models in literature.

Authors	**Weibull Slope**
Lundberg-Palmgren [7]	1.125
Raje et al. [15]	3.36
Paulson et al. [22]	1.18
Weinzapfel et al. [87]	4.55
Vijay et al. [23]	0.95

partition based on the voxelization of a Voronoi tesselation of the half-space is proposed. The half-space is then filled with multiple cuboidal inclusions having the same cubic elastic properties but random material orientations. The model allow to take into account the microstructure of the material on the contact pressure distribution and the subsurface stress fields during repeated rolling cycles. The main advantage of this method is the coupled resolution of both the contact problem and the heterogeneous subsurface problem. One of the limitation of the method is the non smooth representation of grain boundaries due to the voxelization technique. It can lead to some numerical stress gradients [92]. The proposed model is applied to investigate the scatter in fatigue life of rolling elements bearings and compared to results obtained with Finite Elements simulations.

5. Acknowledgements

The authors acknowledge Safran Aircraft Engines for providing the financial support of this project and for giving permission to publish this work. The authors also acknowledge the ANRT for providing the CIFRE grant allowing us to achieve this work.

References

[1] T. A. Harris, Rolling bearing analysis, John Wiley and Sons, 2001.

Nomenclature

Letters

b	contact half width
B^*_{ijkl}	influence coefficients that relating the stress σ_{ij} at point (x, y, z) to the constant eigenstrain at the point (x^k, y^k, z^k)
C^M_{ijkl}, C^I_{ijkl}	elastic constants of the matrix and the inhomogeneity
E^I	Young's modulus of the inhomogeneity
H	hardness of the material
h	distance between the two surfaces of the contacting bodies
I_{ijkl}	the fourth-order identity tensor
K^n	coefficients in the normal displacement at the contact surface due to the contact pressure
M_{ij}	influence coefficients relating the stress σ_{ij} at the point (x, y, z) to the normal traction σ^n within a discretized area centered at $(x^k_1, x^k_2, 0)$
n_x, n_y, n_z	grid sizes in the half-space along the Cartesian directions x, y, z, respectively
W	normal applied load
P_0	maximum Hertzian pressure
P	contact pressure distribution
R	indenter radius
S_{ijkl}	components of the Eshelby's tensor
u^0_i	displacements corresponding to the infinite applied strain ε^0_{ij}
u_i	disturbed contribution of the displacements
$x^I = (x^I, y^I, z^I)$	cartesian coordinates of the inclusion center
N	number of cycles
N_i	number of inclusions in the enrichment along direction i.

Greek letters

ε^0_{ij}	infinite applied strain
ε_{ij}	strain due to eigenstrains
ε^*_{ij}	eigenstrain due to the presence of inhomogeneities
σ^0_{ij}	stress corresponding to the infinite applied strain ε^0_{ij}
σ_{ij}	disturbed contribution of the stresses
δ_{ij}	kronecker symbol
σ^n	normal pressure due to the summution of both symmetric inclusions

[2] W. E. Littmann, R. L. Widner, Propagation of contact fatigue from surface and subsurface origins, Journal of Basic Engineering 88 (1966) 624–636.

[3] D. Nelias, M.-L. Dumont, F. Champiot, A. Vincent, D. Girodin, R. Fougéres, L. Flamand, Role of inclusions, surface roughness and operating conditions on rolling contact fatigue, Journal of Tribology 121 (2) (1999) 240–251.

[4] D. Nelias, M.-L. Dumont, F. Couhier, G. Dudragne, L. Flamand, Experimental and theoretical investigation on rolling contact fatigue of 52100 and M50 steels under EHL or micro-EHL conditions, Journal of Tribology 120 (2) (1998) 184–190.

[5] F. Sadeghi, B. Jalalahmadi, T. Slack, N. Raje, N. Arakere, A review of rolling contact fatigue, Journal of Tribology 131 (2009) 041403–1.

[6] W. Weibull, A statistical theory of the strength of materials, Royal Swedish Academy of Engineering Sciences Proc. 151 (1939) 4–45.

[7] G. Lundberg, A. Palmgren, Dynamic capacity of rolling bearings, Acta Polytechnica, Mechanical Engineering Series 2 1 (3) (1947) 7–53.

[8] R. S. Zhou, Surface topography and fatigue life of rolling contact bearings, Tribology Transactions 36 (1993) 329–340.

[9] E. V. Zaretsky, Design for life, plan for death, Machine Design 66 (15) (1994) 55–59.

[10] W. Cheng, H. S. Cheng, Semi-analytical modeling of crack initiation dominant contact fatigue for roller bearings, in: Proceedings of the 1995 Joint ASME/STLE Tribology Conference, Orlando, FL, Oct. 8-11., 1995.

[11] T. A. Harris, W. K. Yu, Lundberg-palmgren fatigue theory: Considerations of failure stress and stressed volume, Journal of Tribology 121 (1) (1999) 85–89.

[12] G. E. Morales-Espejel, A. Gabelli, A model for gear life with surface and subsurface survival: Tribological effects, Wear 404-405 (2018) 133–142.

[13] L. Chen, Q. Chen, E. Shao, Study on initiation and propagation angles of sub-surface cracks in GCr15 bearing steel under rolling contact, Wear 133 (1989) 205–218.

[14] T. Yoshioka, Detection of rolling contact sub-surface fatigue cracks using acoustic emission technique, Lubrication Engineering 49 (4) (1993) 303–308.

[15] N. Raje, F. Sadeghi, R. G. Rateick, A statistical damage mechanics model for subsurface initiatied spalling in rolling contacts, Journal of Tribology 130 (4) (2008) 042201.

[16] K. Nakazawa, G. Krauss, Microstructure and fracture of 52100 steel, Metallurgical Transactions A 9 (5) (1978) 681–689.

[17] O. Ito, E. R. Fuller, Computer modelling of anisotropic grain microstructure in two dimensions, Acta Metallurgica Materialia 41 (1993) 191–198.

[18] S. Kumar, S. K. Kurtz, Simulation of material microstructure using a 3D voronoi tessellation: Calculation of effective thermal expansion coefficient of polycrystalline materials, Acta Metallurgica Materialia 42 (12) (1994) 3917–3927.

[19] M. Nygårds, P. Gudmundson, Three-dimensional periodic voronoi grain models and micromechanical fe-simulations of a two-phase steel, Computer Materials Science 24 (4) (2002) 513–519.

[20] N. Raje, F. Sadeghi, R. G. Rateick, G. Richard, M. R. Hoeprich, A numerical model for life scatter in rolling element bearings, Journal of Tribology 130 (2008) 011011.

[21] N. Weinzapfel, F. Sadeghi, V. Bakolas, An approach for modeling material grain structure in investigations of hertzian subsurface stresses and rolling contact fatigue, Journal of Tribology 132 (2010) 041404–1.

[22] N. R. Paulson, J. A. R. Bomidi, F. Sadeghi, R. D. Evans, Effects of crystal elasticity on rolling contact fatigue, International Journal of Fatigue 61 (2014) 67–75.

[23] A. Vijay, K. Paulson, F. Sadeghi, A 3D finite element modelling of crystalline anisotropy in rolling contact fatigue, International Journal of Fatigue 106 (2018) 92–102.

[24] N. R. Paulson, F. Sadeghi, EHL modeling of nonhomogeneous materials: The effects of polycristalline anisotropy on RCF, Tribology International 112 (2017) 137–146.

[25] T. Dick, G. Cailletaud, Fretting modelling with a crystal plasticity model of Ti6Al4V, Computational Materials Science 38 (1) (2006) 113–125.

[26] M. Zhang, R. W. Neu, D. L. McDowell, Microstructure-sensitive modeling: Application to fretting contacts, International Journal of Fatigue 31 (8-9) (2009) 1397–1406.

[27] P. J. Ashton, A. M. Harte, S. B. Leen, Statistical grain size effects in fretting crack initiation, Tribology International 108 (2017) 75–86.

[28] A. Warhadpande, B. Jalalahmadi, T. Slack, F. Sadeghi, A new finite element fatigue modeling approach for life scatter in tensile steel specimens, International Journal of Fatigue 32 (4) (2010) 685–697.

[29] A. Ghosh, B. D. Leonard, F. Sadeghi, A stress based damage mechanics model to simulate fretting wear of hertzian line contact in partial slip, Wear 307 (2013) 87–99.

[30] A. Ghosh, W. Wang, F. Sadeghi, An elastic-plastic investigation of third body effects on fretting contact in partial slip, International Journal of Solids and Structures 81 (2016) 95–109.

[31] A. Brandt, A. A. Lubrecht, Multilevel matrix multiplication and fast solution of integral equations, Journal of Computational Physics 90 (2) (1990) 348–370.

[32] H. Boffy, C. H. Venner, Multigrid solution of 3D stress field in strongly hetergeneous materials, Tribology International 74 (2014) 121–129.

[33] H. Boffy, C. H. Venner, Multigrid numerical simulation of contact mechanics of elastic materials with 3D heterogeneous subsurface topology, Tribology International 92 (2015) 233–245.

[34] A. Vijay, F. Sadeghi, A continuum damage mechanics framework for modeling the effect of crystalline anisotropy on rolling contact fatigue, Tribology International 140 (2019) 105845.

[35] M. Ghodrati, M. Ahmadian, R. Mirzaeifar, Three-dimensional study of rolling contact fatigue using crystal plasticity and cohesive zone method, International Journal of Fatigue 128 (2019) 105208.

[36] K. Singh, F. Sadeghi, M. Correns, Blass, A microstructure based approach to model effects of surface roughness on tensile fatigue, International Journal of Fatigue 129 (2019) 105229.

[37] G. Vouaillat, J. Noyel, F. Ville, X. Kleber, S. Rathery, From hertzian contact to spur gears : analyses of stresses and rolling contact fatigue, Mechanics & Industry 20 (2019) 626.

[38] H. Zhou, P. Wei, H. Liu, C. Zhu, C. Lu, G. Deng, Roles of microstructure, inclusions and surface roughness on rolling contact fatigue of a wind turbine gear, Fatigue and Fracture of Engineering Materials and Structures (2020) 1–16.

[39] E. Bossy, J. Noyel, X. Kleber, F. Ville, C. Sidoroff, S. Thibault, Competition between surface and subsurface rolling contact fatigue failures of nitrided parts: A dang van approach, Tribology International 140 (2019) 105888.

[40] C. Jacq, D. Nelias, G. Lormand, D. Girodin, Development of a three-dimensional semi-analytical elastic-plastic contact code, Journal of Tribology 124 (4) (2002) 653–667.

[41] V. Boucly, D. Nelias, S. Liu, Q. Wang, L. M. Keer, Contact analyses for bodies with frictional heating and plastic behavior, Journal of Tribology 127 (2005) 355–364.

[42] L. Gallego, D. Nelias, C. Jacq, A comprehensive method to predict wear and to define the optimum geometry of fretting surfaces, Journal of Tribology 128 (2006) 476–485.

[43] D. Nelias, D. Antaluca, V. Boucly, Rolling of an elastic ellipsoid upon an elastic-plastic flat, Journal of Tribology 129 (4) (2007) 791–800.

[44] L. Gallego, D. Nelias, Modeling of fretting wear under gross slip and partial slip conditions, Journal of Tribology 129 (3) (2007) 528–535.

[45] L. Gallego, D. Nelias, S. Deyber, A fast and efficient contact algorithm for fretting problems applied to fretting modes i, ii and iii, Wear 268 (1) (2010) 208–222.

[46] V. Done, D. Kesavan, R. Murali Krishna, T. Chaise, D. Nelias, Semi analytical fretting wear simulation including wear debris, Tribology International 109 (2017) 1–9.

[47] F. Wang, L. Keer, Numerical simulation for three-dimensional elastic-plastic conact with hardening behavior, Journal of Tribology 127 (3) (2005) 494–502.

[48] W. W. Chen, Q. J. Wang, F. Wang, L. M. Keer, J. Ciao, Three-dimensional repeated elasto-plastic point contacts, rolling, and sliding, Journal of Applied Mechanics 75 (2008) 021021.

[49] K. Zhou, W. Chen, L. M. Keer, Q. Wang, A fast method for solving three-dimensional arbitrarily shaped inclusions in a half space, Computer Methods in Applied Mechanics and Engineering 198 (9-12) (2009) 885–892.

[50] B. Fulleringer, D. Nelias, On the tangential displacement of a surface point due to a cuboid of uniform plastic strain in a half-space, Journal of Applied Mechanics 77 (2) (2010) 021014–1/7.

[51] K. Zhou, W. Chen, L. M. Keer, X. Ai, K. Sawamiphakdi, P. Glaws, Q.Wang, Multiple 3D inhomogeneous inclusions in a half space under contact loading, Mechanics of Materials 43 (2011) 444–457.

[52] K. Zhou, L. M. Keer, Q. J. Wang, Semi-analytic solution for multiple interacting three-dimensional inhomogeneous inclusions of arbitrary shape in an infinite space, International Journal for Numerical Methods in Engineering 87 (2011) 617–638.

[53] K. Zhou, L. M. Keer, Q. J. Wang, X. Ai, K. Sawamiphakdi, P. Glaws, Interaction of multiple inhomogeneous inclusions beneath surface, Computer Methods in Applied Mechanics and Engineering 217-220 (2012) 25–33.

[54] J. Leroux, B. Fulleringer, D. Nelias, Contact analysis in presence of spherical inhomogeneities within a half-space, International Journal of Solids and Structures 47 (2010) 3034–3049.

[55] J. Leroux, D. Nelias, Stick-slip analysis of a circular point contact between a rigid sphere and a flat unidirectional composite with cylindrical fibers, International Journal of Solids and Structures 48 (2011) 3510–3520.

[56] K. E. Koumi, D. Nelias, T. Chaise, A. Duval, Modeling of the contact between a rigid indenter and a heteregeneous viscoelastic material, Mechanics of Materials 77 (2014) 28–42.

[57] K. E. Koumi, L. Zhao, J. Leroux, T. Chaise, D. Nelias, Contact analysis in the presence of an ellipsoidal inhomogeneity within a half space, International Journal of Solids and Structures 51 (2014) 1390–1402.

[58] K. E. Koumi, T. Chaise, D. Nelias, Rolling contact of a rigid sphere/sliding of a spherical indenter upon a viscoelastic half-space containing an ellipsoidal inhomogeneity, Journal of the Mechanics and Physics of Solids 80 (2015) 1–25.

[59] K. V. Amuzuga, T. Chaise, A. Duval, D. Nelias, Fully coupled resolution of heterogeneous elastic-plastic contact problem, Journal of Tribology 138 (2016) 021403–1.

[60] Q. Dong, K. Zhou, W. W. Chen, Q. Fan, Partial slip contact modeling of heterogeneous elasto-plastic materials, International Journal of Mechanical Sciences 114 (2016) 98–110.

[61] T. Chaise, D. Nelias, Contact pressure and residual strain in 3D elasto-plastic rolling contact for a circular or elliptical point contact, Journal of Tribology 133 (4) (2011) 041402.

[62] T. Chaise, J. Li, D. Nelias, R. Kubler, S. Taheri, G. Douchet, V. Robin, P. Gilles, Modelling of multiple impacts for the prediction of distortions and residual stresses induced by ultrasonic shot peening (USP), Journal of Materials Processing Technology 212 (2012) 2080–2090.

[63] T. Chaise, D. Nelias, F. Sadeghi, On the effect of isotropic hardening on the coeffcient of restitution for single or repeated impacts using a semi-analytical method, Tribology Transactions 54 (5) (2011) 714–722.

[64] C. Bagault, D. Nelias, M.-C. Baietto, Contact analyses for anisotropic half space: Effect of the anisotropy on the pressure distribution and contact area, Journal of Tribology 134 (3) (2012) 031401.

[65] C. Bagault, D. Nelias, M.-C. Baietto, T. Ovaert, Contact analyses for anisotropic half-space coated with an anisotropic layer: Effect of the anisotropy on the pressure distribution and contact area, International Journal of Solids and Structures 50 (5) (2013) 743–754.

[66] Y. Gao, S. Kim, S. Zhou, H.-C. Chiu, D. Nelias, C. Berger, W. De Heer, L. Polloni, R. Sordan, A. Bongiorno, E. Riedo, Elastic coupling between layers in two-dimensional materials, Nature Materials 14 (7) (2015) 714–720.

[67] D. Li, Z. Wang, Q. Wang, Explicit analytical solutions for elastic fields in two imperfectly bonded half-spaces with a thermal inclusion, International Journal of Engineering Science 135 (2019) 1–16.

[68] X. Zhang, Q. J. Wang, Y. Wang, Z. Wang, H. Shen, J. Liu, Contact involving a functionally graded elastic thin film and considering surface effects, International Journal of Solids and Structures 150 (2018) 184–196.

[69] D. Li, Z. Wang, H. Yu, Q. Wang, Elastic fields caused by eigenstrains in two joined half-spaces with an interface of coupled imperfections: Dislocation-like and force-like conditions, International Journal of Engineering Science 126 (2018) 22–52.

[70] T. Beyer, T. Chaise, J. Leroux, D. Nelias, A damage model for fretting contact between a sphere and a half space using semi-analytical method, International Journal of Solids and Structures 164 (2019) 66–83.

[71] T. Beyer, F. Sadeghi, T. Chaise, J. Leroux, D. Nelias, A coupled damage model and a semi-analytical contact solver to simulate butterly wing formation around nonmetallic inclusions, International Journal of Fatigue 127 (2019) 445–460.

[72] N. Ren, D. Zhu, W. W. Chen, Y. Liu, Q. J. Wang, A three-dimensional deterministic model for rough surface line-contact EHL problems, Journal of Tribology 131 (2009) 011501–1.

[73] Z. Wang, D. Zhu, Q. Wang, Elastohydrodynamic lubrication of inhomogeneous materials using the equivalent inclusion method, Journal of Tribology 136 (2) (2013) 021501.

[74] Z. Shengguang, W. Wenzhong, Z. Ziqiang, Elastohydrodynamic lubrication analysis of point contact with consideration of material inhomogeneity, Journal of Tribology 136 (4) (2014) 041501.

[75] K. Zhou, Q. Dong, A three-dimensional model of line-contact elastohydrodynamic lubrication for heterogeneous materials with inclusions, International Journal of Applied Mechanics 8 (2) (2016) 1650014.

[76] Z. A. Moschovidis, T. Mura, Two-ellipsoidal inhomogeneities by the equivalent inclusion method, Journal of Applied Mechanics 42 (1975) 847–852.

[77] S. Liu, Q. Wang, G. Liu, A versatile method of discrete convolution and FFT (DC-FFT) for contact analyses, Wear 243 (1-2) (2000) 101–111.

[78] S. Liu, Q. Wang, Studying contact stress fields caused by surface tractions with a discrete convolution and fast fourier transform algorithm, Journal of Tribology 124 (1) (2002) 36–45.

[79] Y. P. Chiu, On the stress field and surface deformation in a half space with a cuboidal zone in which initial strains are uniform, Journal of Applied Mechanics 45 (1978) 302–306.

[80] A. Okabe, B. Boots, K. Sugihara, S. N. Chiu, Spatial Tessellations: Concepts and Applications of Voronoi Diagrams, Wiley, West Sussex, UK., 2000.

[81] C. B. Barber, D. P. Dobkin, H. T. Huhdanpaa, The quickhull algorithm for convex hulls, ACM Transactions on Mathematical Software 22 (4) (1996) 469–483.

[82] L. Vitos, P. A. Korzhavyi, B. Johansson, Stainless steel optimization from quantum mechanical calculations, Nature Materials 2 (2003) 25–28.

[83] J. A. R. Bomidi, N. Weinzapfel, F. Sadeghi, T. Slack, S. M. Moghaddam, A. Liebel, J. Weber, T. Kreis, Experimental and numerical investigation of torsion fatigue of bearing steel, Journal of Tribology 135 (3) (2013) 031103.

[84] L. Zhao, D. Nelias, D. Bardel, A. Maynadier, P. Chaudet, B. Marie, On the fracture of multi-crystalline silicon wafer, Journal of Physics D: Applied Physics 49 (47) (2016) 475–601.

[85] P. Peralta, A. Schober, C. Laird, Elastic stresses in anisotropic bicrystals, Materials Science & Engineering, A: Structural Materials: Properties, Microstructure and Processing 169 (1993) 43–51.

[86] B. Jalalahmadi, F. Sadeghi, A voronoi finite element study of fatigue life scatter in rolling contacts, Journal of Tribology 131 (2) (2009) 022203–1/15.

[87] N. Weinzapfel, F. Sadeghi, V. Bakolas, A. Liebel, A 3D finite element study of fatigue life dispersion in rolling line contacts, Journal of Tribology 133 (4) (2011) 042202–1/10.

[88] A. Warhadpande, F. Sadeghi, M. N. Kotzalas, G. Doll, Effects of plasticity on subsurface initiated spalling in rolling contact fatigue, International Journal of Fatigue 61 (2014) 67–75.

[89] Z. Golmohammadi, A. Walvekar, F. Sadeghi, A 3D efficient finite element model to simulate rolling contact fatigue under high loading conditions, Tribology International 126 (2018) 258–269.

[90] S. M. Moghaddam, F. Sadeghi, K. Paulson, N. Weinzapfel, M. Correns, M. Dinkel, A 3D numerical and experimental investigation of microstructural alterations around non-metallic inclusions in bearing steel, International Journal of Fatigue 88 (2016) 29–41.

[91] D. R. Thoman, L. J. Bain, C. E. Antler, Maximum likelihood estimation, exact confidence intervals for reliability and tolerance limits in the weibull distribution, Technometrics 12 (1970) 363–371.

[92] A. Doitrand, C. Fagiano, F.-X. Irisarri, M. Hirsekorn, Comparison between voxel and consistent meso-scale models of woven composites, Composites: Part A 73 (2015) 143–154.

[93] K. Johnson, Contact Mechanics, Press syndicate of the university of Cambridge, 1985.

Appendix A. Stress in a half-space due to a concentrated unit normal force at the surface origin(F_{ij})

$$F_{11}(x,y,z) = \frac{1}{2\pi}\left[\frac{1-2\nu}{r^2}(1-\frac{z}{\rho})\frac{x^2-y^2}{r^2} + \frac{zy^2}{\rho^3} - \frac{3zx^2}{\rho^5}\right],$$

$$F_{22}(x,y,z) = F_{11}(y,x,z),$$

$$F_{33}(x,y,z) = -\frac{3}{2\pi}\frac{z^3}{\rho^5},$$

$$F_{12}(x,y,z) = \frac{1}{2\pi}\left[\frac{1-2\nu}{r^2}(1-\frac{z}{\rho})\frac{xy}{r^2} + \frac{zyx}{\rho^3} - \frac{3zyx}{\rho^5}\right],$$

$$F_{13}(x,y,z) = -\frac{3}{2\pi}\frac{xz^2}{\rho^5},$$

$$F_{23}(x,y,z) = F_{12}(y,x,z),$$

where

$$r^2 = x^2+y^2, \quad \rho = \sqrt{x^2+y^2+z^2},$$

with ν, the Poisson's ratio of the isotropic half-space.

Appendix B. Stresses in a half-space subject to normal pressure (M_{ij})

An isotropic half-space is submitted a uniform normal pressure σ^n in a discretized surface area of $2\Delta x \times 2\Delta y$ at the center point $P(x',y',0)$. The stress at an observation point $Q(x,y,z)$ is given in [49] and [93]:

$$\begin{aligned}\sigma_{ij}(x,y,z) &= M_{ij}(x-x',y-y',z)\sigma^n(x,y)\\ \sigma_{ij}(x,y,z) &= \frac{\sigma^n}{2\pi}[h_{ij}(\xi_1+\Delta x,\xi_2+\Delta y,\xi_3) - h_{ij}(\xi_1+\Delta x,\xi_2-\Delta y,\xi_3)\\ &\quad + h_{ij}(\xi_1-\Delta x,\xi_2-\Delta y,\xi_3) - h_{ij}(\xi_1-\Delta x,\xi_2+\Delta y,\xi_3)]\end{aligned}$$

where

$$\xi_1 = x - x'.\xi_2 = y - y'.\xi_3 = z - z'.$$

The functions $h_{ij}()$ in Eq.(B1) are defined by

$$h_{11}(x,y,z) = 2\nu \tan^{-1} \frac{y^2+z^2-\rho y}{xz} + 2(1-\nu)\tan^{-1}\frac{\rho - y + z}{x} + \frac{xyz}{\rho(x^2+z^2)},$$

$$h_{22}(x,y,z) = h_{11}(y,x,z),$$

$$h_{33}(x,y,z) = \tan^{-1}\frac{y^2+z^2-\rho y}{xz} - \frac{xyz}{\rho}\left(\frac{1}{x^2+z^2} + \frac{1}{y^2+z^2}\right),$$

$$h_{12}(x,y,z) = -\frac{z}{\rho} - (1-2\nu)\log(\rho+z),$$

$$h_{13}(x,y,z) = -\frac{yz^2}{\rho(x^3+z^2)},$$

$$h_{23}(x,y,z) = h_{13}(y,x,z),$$

where

$$rho = \sqrt{x^2+y^2+z^2}.$$

Appendix C. Normal displacement at the surface subject to normal pressure (K^n)

The contact between a sphere and an elastic half-space having respectively elastic constants (E_1, ν_1) and (E_2, ν_2), where the surface $z = 0$ is discretized into rectangular surface area of $2\Delta_1 \times 2\Delta_2$, is now considered. The initial contact point coincides with the origin of the Cartesian coordinate system $((x, y, z)$. The relationship between the normal displacement at an observation point $P(\xi_1, \xi_2, 0)$ and the pressure field at the center $Q(\xi_1', \xi_2', 0)$ is built using the function K^n.

$$K^n(c_1,c_2) = \left[\frac{1-\nu_1^2}{\pi E_1} + \frac{1-\nu_2^2}{\pi E_2}\right]\sum_{p=1}^{4} K_p^n(c_1,c_2),$$

$$K_1^n(c_1,c_2) = (c_1+\Delta_1)\log\left(\frac{(c_2+\Delta_2)+\sqrt{(c_2+\Delta_2)^2+(c_1+\Delta_1)^2}}{(c_2-\Delta_2)+\sqrt{(c_2-\Delta_2)^2+(c_1+\Delta_1)^2}}\right),$$

$$K_2^n(c_1,c_2) = (c_2+\Delta_2)\log\left(\frac{(c_1+\Delta_1)+\sqrt{(c_2+\Delta_2)^2+(c_1+\Delta_1)^2}}{(c_1-\Delta_1)+\sqrt{(c_2+\Delta_2)^2+(c_1-\Delta_1)^2}}\right),$$

$$K_3^n(c_1,c_2) = (c_1-\Delta_1)\log\left(\frac{(c_2-\Delta_2)+\sqrt{(c_2-\Delta_2)^2+(c_1-\Delta_1)^2}}{(c_2+\Delta_2)+\sqrt{(c_2+\Delta_2)^2+(c_1-\Delta_1)^2}}\right),$$

$$K_4^n(c_1,c_2) = (c_2-\Delta_2)\log\left(\frac{(c_1-\Delta_1)+\sqrt{(c_2-\Delta_2)^2+(c_1-\Delta_1)^2}}{(c_1+\Delta_1)+\sqrt{(c_2-\Delta_2)^2+(c_1+\Delta_1)^2}}\right),$$

where

$$c_1 = \xi_1 - \xi_1' \quad \text{and} \quad c_2 = \xi_2 - \xi_2'$$